




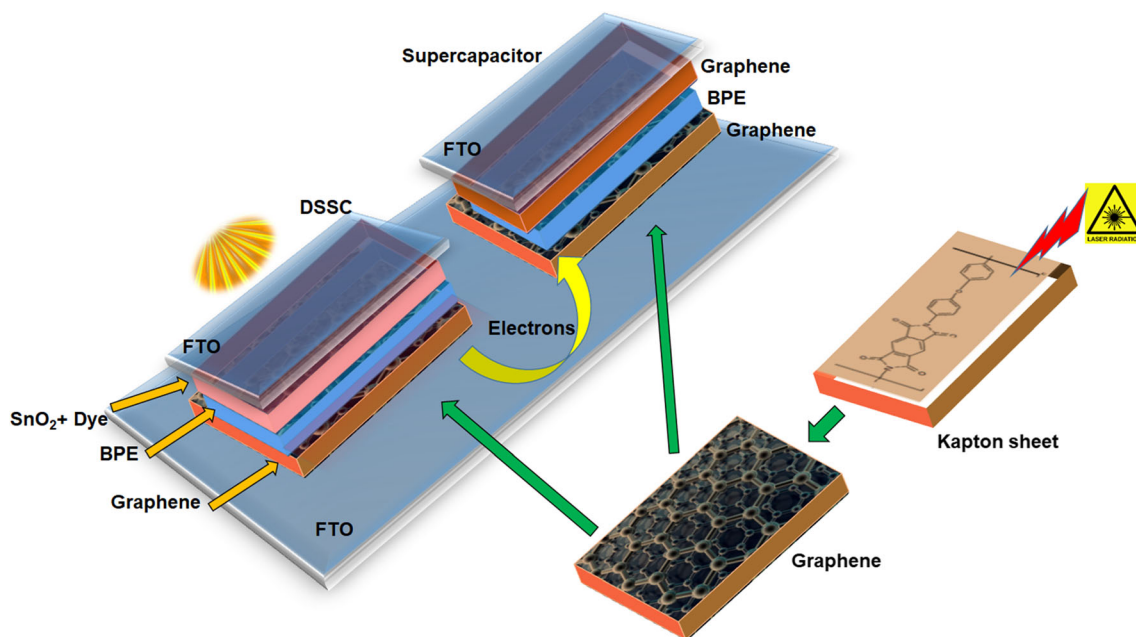
Conductivity/Electrochemical Study of Polyvinyl pyrrolidone-Poly(vinyl alcohol)/I₃⁻ Thin Film Electrolyte for Integrated Dye-Sensitized Solar Cells and Supercapacitors

D.N. SANGEETHA,¹ NIVEDITHA HEGDE,¹ VIDYASHRI POOJARI,¹
DHEERAJ DEVADIGA,¹ Y.N. SUDHAKAR,² M.S. SANTOSH,³
and M. SELVAKUMAR ^{1,4}

1.—Department of Chemistry, Manipal Institute of Technology, Manipal Academy of Higher Education, Manipal, Karnataka 576104, India. 2.—Department of Chemistry, Christ (Deemed to be University), Bangalore Dharmaram Campus, Bengaluru, Karnataka 560029, India. 3.—Centre for Incubation, Innovation, Research, and Consultancy (CIIRC), Jyothy Institute of Technology, Thataguni, Bangalore, Karnataka 560082, India. 4.—e-mail: chemselva@rediffmail.com

The current era focuses not only on producing solar energy but also preserving it for future use. Dye-sensitized solar cells (DSSC) and supercapacitors (SC) are such energy-based devices. DSSCs capture the solar energy and SCs store this captured energy. A natural anthocyanin dye extracted from *Garcinia indica* (kokum fruit) was used in the DSSCs. SnO₂, one of the promising electrode materials for DSSC, was synthesized via a microwave technique. Blend polymer electrolytes (BPE) were prepared through a solution casting technique. A polyvinyl pyrrolidone (PVP) and polyvinyl alcohol (PVA) blend with varying concentrations of potassium iodide, along with iodine dopant, was prepared as a BPE electrolyte composition. The best of the PVA-PVP/KI composition was chosen using Nyquist plots of electrochemical impedance spectroscopy (EIS). Varying the temperature, the dielectric and conductivity study of the chosen composition was studied in detail. A fast/single-step synthesis technique, namely a laser-engraved approach, was used for few-layer graphene synthesis. This graphene serves as a common platform for the DSSC-SC integrated device: as a counter electrode in DSSC and graphene-graphene symmetric electrode in SC. A DSSC-SC integrated device was fabricated and characterized using various analytical and microscopy techniques. The integrated device showed a 0.42 fill factor and 0.56% efficiency. The discharge time for integrated DSSC-SC cells was found to be increased threefold.

Graphical Abstract



Key words: Dye-sensitized solar cell, supercapacitor, blend polymer electrolyte

INTRODUCTION

A more efficient system for conversion and storage of energy has become important with the advancement of modern electronics. Dye-sensitized solar cells (DSSCs) serve this purpose. DSSC, the third generation of solar cells, is a photovoltaic cell that entraps abundantly available solar energy and converts it into electrical energy.¹ Being semi-transparent and operating even under low-light conditions, these are regarded as cost-effective and eco-friendly.² DSSCs generally have a photosensitive dye with TiO_2 as a photoanode and a platinum counter electrode. An electrolyte is sandwiched between the anode and cathode.³ A supercapacitor (SC) is an energy storage unit that connects conventional dielectric capacitors with rechargeable batteries. Their application is in those fields demanding faster charge-discharge cycles instead of long-time energy storage, high power density, and long life cycle.⁴

SnO_2 is an important n-type semiconductor with a bandgap of 3.6 eV and high stability in strong acids/bases, and is often referred to as a good oxidizing agent. It has been used in several applications such as optoelectronic devices: as cathode materials in lithium batteries and supercapacitors. SnO_2 is the most popular material for light-conductive films and

solar cells, due to its capacity to absorb infrared light and transmit visible light.⁵ SnO_2 is used as a photoanode for DSSC. Upon light illumination on SnO_2 , the electrons are excited from the valence to the conduction band. With SnO_2 , faster transfer of these excited electrons to the conduction band from the excited dye molecule takes place. Among several synthesis approaches, the microwave technique was chosen in the current study. This method enables product formation within a short period.

The next component of the DSSC is the counter electrode. Pt as the counter electrode is most widely used. The cost and availability, however, limit the usability. Graphene was identified as an alternative for the Pt as a counter electrode. As a strong conducting substance, it is used in a variety of energy applications,^{6–8} including DSSC.^{9,10} Conventional graphene synthesis requires various chemicals and several steps, which is time-consuming. Laser-induced graphene (LIG) synthesis is a prominent method for producing high-density graphene in a short period of time.^{11–13} A polyimide film, Kapton, is used as a precursor for graphene synthesis. Laser-engraved graphene (LEG) is a result of the photothermal effect. The high-energy laser irradiation results in lattice vibration, which leads to extremely high temperatures. At this high temperature, the C-O, C=O, and N-C bonds of polyimide

are easily broken. This was verified by decreasing the content of nitrogen and oxygen in LIG, and these atoms are released as gases and converted to graphitic structures.

In DSSC, photosensitizing dyes play an important role in light absorption and injection of the excited electrons into the semiconductor's conduction bands. The synthetic organic dye/sensitizer shows a broad and strong absorption in UV-visible light.^{14,15} Nevertheless, their practical use is constrained by high costs, difficulty in synthesizing, and toxicity. Owing to their cost-effectiveness, ease of accessibility, abundant raw materials, and easy extraction methods, natural dyes can replace synthetic organic dyes. In this study, kokum-based anthocyanin dye was used as a photosensitizer.

Another material to consider in device fabrication is the electrolyte. The electrolyte functions to produce ionic conductivity between the positive-negative electrodes in an electrochemical device. Also, the electrolyte in the DSSC restores the original state of dye through the donation of electrons. Traditionally, liquid electrolytes are used in DSSCs and SCs but have certain disadvantages such as electrode corrosion and solvent evaporation. Polymer-based electrolytes have recently been used to overcome the problems associated with liquid-based electrolytes.¹⁶⁻¹⁹ Solvent-free polymer electrolytes are a new type of solid ionic conductor. The present work uses iodine-doped poly(vinyl alcohol)/polyvinyl pyrrolidone (PVA-PVP) polymer blended electrolytes. The PVP-PVA are eco-friendly and biodegradable polymers.²⁰ The primary reason for choosing the blended polymer electrolyte is to increase the conductivity. The blend polymer is physically identical to but structurally different from the individual polymers. The blended polymer has hydrogen bond interlinking and ionic and dipole interactions and can easily increase the ionic conductivity.

The current study focuses on integrating DSSC with laser-induced graphene-based SC for energy harvesting and storage.^{21,22} Graphene serves as a common platform for DSSCs and SCs. In order to monitor the performance of this integrated device, it was subjected to I-V characterization, charge-discharge, and cyclic voltammetry studies.

EXPERIMENTAL

Preparation of Natural Photosensitizer

Garcinia indica, also referred to as kokum, is a natural photosensitizing anthocyanin dye. By taking 10 g of dry kokum rind in 100 ml of water and soaking it for 5 h, a photosensitizer dye was prepared. The pigment in the kokum dispersed into the water, yielding a deep red color. The dye extract was filtered and stored in a dark bottle, and the kokum rind was discarded.

Synthesis of Tin Oxide (SnO₂)

Tin (II) chloride (SnCl₂·H₂O) and hydrazine hydrate were diluted in deionized water. A typical experimental procedure is as follows. (SnCl₂·H₂O) and hydrazine hydrate at a molar ratio of 1:3 were mixed under stirring. The pH of the solution was maintained within 7 to 9 using hydrazine hydrate. The resulting mixture was then placed in a domestic microwave for 30 min under high radiation. The light gray precipitate obtained was filtered, washed several times with deionized water until no chloride ions were detected, and then dried for 4 h at 80°C.

Preparation of Blend Polymer Electrolyte

A blend polymer electrolyte (BPE) stock solution was prepared by mixing 500 mg of polyvinyl pyrrolidone and poly(vinyl alcohol) (PVP-PVA) in a minimum amount of water. The stock solutions were mixed in a ratio of 60:40 with different wt.% of potassium iodide (KI) and iodine (I₂) to obtain a total volume of 10 mL under continuous stirring. The *x* wt.% of KI (where *x* = 20, 25, 30, and 35) in the PVP-PVA: KI mixture was varied while the weight of I₂ was fixed at 10 wt.% of KI in all the samples. The mixture was stirred well in a beaker and then poured into a petri dish and dried in an oven to obtain BPE.

Synthesis of Graphene

Kapton sheets were used as a precursor for graphene synthesis. The Kapton sheets were cut into an area of 5 cm² and mounted in a laser engraving machine. A CO₂ laser beam was focused on the sheet for engraving to form graphene material on the surface. For the complete engraving process, the software applied a laser power of 50 W at a speed of 600 dpi for 15 min. Black powder was finally obtained as graphene.

Fabrication of DSSC

First, 0.45 g of SnO₂ was dispersed in 3 mL of water and sonicated for 20 min, and then dispersed in ethanol for 15 min. It was spray-coated on a preheated fluorine-doped tin oxide (FTO) plate. After drying, it was sintered at 150°C for 30 min and was allowed to cool naturally. SnO₂ coated FTO plate was then soaked in the dye extraction and dried for 24 h. This dye-coated SnO₂ on FTO served as the photoanode, and FTO coated with graphene was taken as the counter electrode. The BPE was sandwiched between the photoanode (dye-coated SnO₂ on FTO) and the cathode (graphene-coated FTO) was the DSSC.

Fabrication of Supercapacitor Electrode

Laser-engraved graphene was coated on the FTO substrate using PVDF in NMP (polyvinylidene fluoride in *N*-methyl-2-pyrrolidone) as a binder.

The supercapacitor cell was fabricated using BPE film sandwiched between two graphene-coated FTO electrodes.

Device Characterization

The characterization of DSSC was carried out before exposure to solar radiation and in the presence of sunlight. The efficiency and fill factor of the DSSC were calculated from the I–V plot. The supercapacitor was characterized by AC impedance and galvanostatic charge-discharge studies (GCD).

The photoanode and the graphene-graphene-based supercapacitor were individually separated on the common graphene-coated FTO material by BPE. The setup was an integrated DSSC-supercapacitor device. The characterization of the integrated device was carried out using AC impedance, charge-discharge measurements, and I–V characteristics.

RESULTS AND DISCUSSION

Material Characterization

Figure 1a shows the UV-visible spectra of anthocyanin pigment extracted from kokum. An absorption peak was observed at 520 nm, indicating its absorption range in the visible region. The kokum rind has a red anthocyanin pigment of 2% to 3% and is water-soluble. Methoxy groups account for the reddish color, while the bluish color is due to more of the hydroxyl groups. Cyanidin-3-glucoside and

cyanine-3-sambubioside are the two major pigments found in kokum rinds, usually present in a 4:1 ratio. The chemical combination of glycoside and acyl groups in the basic structure of anthocyanin pigment is responsible for the several-colored compounds.^{23–26}

SnO₂ phase and purity were examined by X-ray diffraction, as shown in Fig. 1b. The diffraction peaks at (110), (111), (021), and (022) planes were assigned to the orthorhombic unit cell ($a = 0.4714$ nm, $b = 0.5727$ nm, and $c = 0.5214$ nm) of SnO₂, and matched well with ICSD card #157450). The orthorhombic phase of SnO₂ was found to be stable only under conditions of high temperature and pressure. Under different conditions, the crystallographic phase changed into a tetragonal rutile structure. In the present case, the microwave used for the synthesis provides high temperature for the completion of the phase, and hence the orthorhombic crystalline structure was obtained. The intermediate tetragonal phase was observed along with the orthorhombic phase. The peaks corresponding to this phase were indexed at the (110), (101), (200), and (211) planes, and they matched well with ICSD card #39173. Thus, the synthesized SnO₂ has a two-phase structure: tetragonal and orthorhombic. The crystallite size was calculated using the Scherrer method and was estimated to be 16.13 nm. Figure 1c and d show the SEM images of SnO₂. The images revealed that the tin oxide synthesized from the microwave-

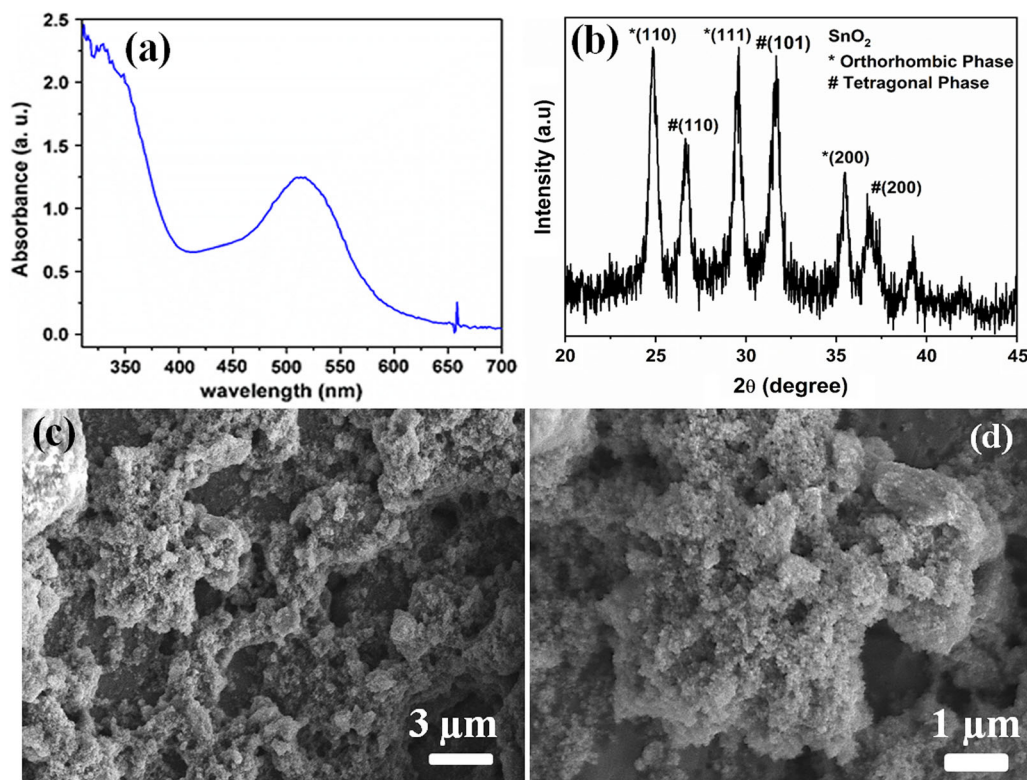


Fig. 1. (a) UV-visible spectra of anthocyanin extracted from kokum; SnO₂ (b) XRD; (c) and (d) SEM.

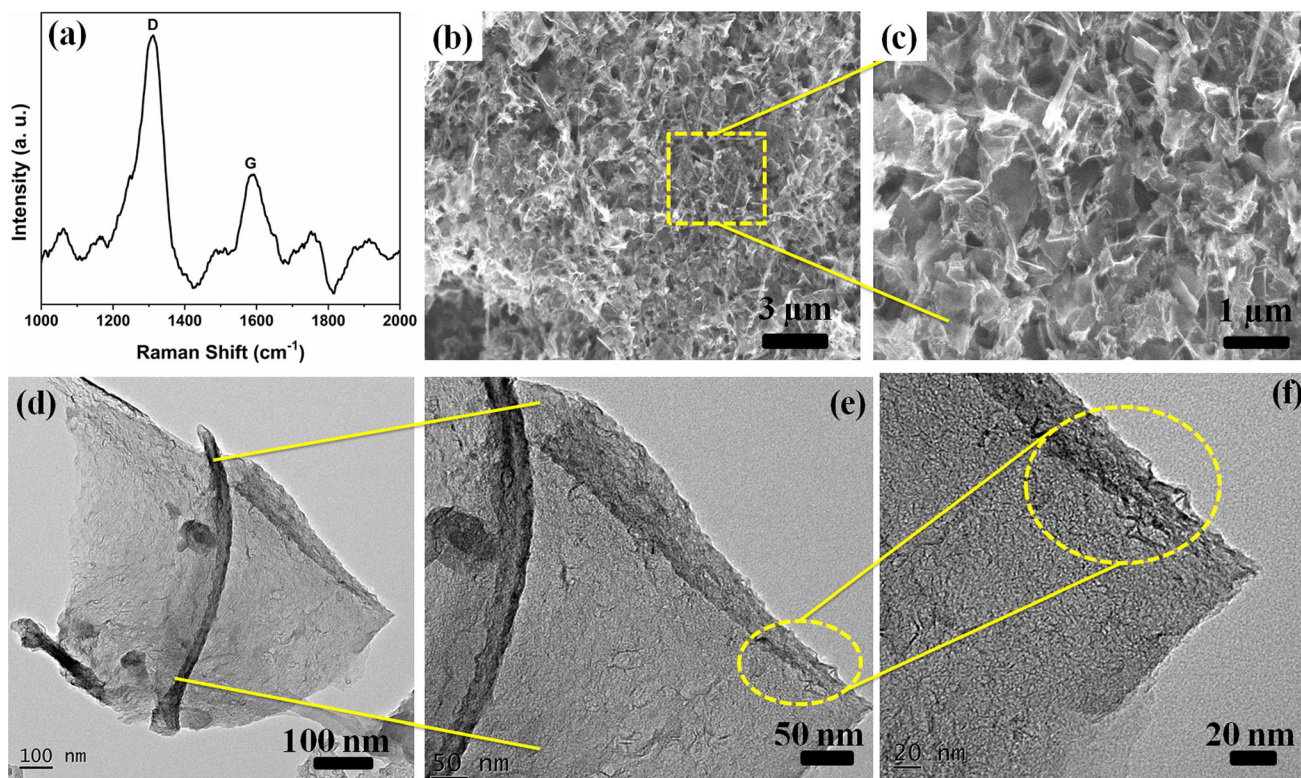


Fig. 2. Laser-engraved graphene. (a) FT-Raman spectra of graphene; (b, c) SEM and (d-f) TEM images.

assisted method showed an orthorhombic nanocrystalline property in the micrographs. The coagulation of microparticles produced the micro-nodes throughout the surface.

The laser-engraved graphene samples were evaluated by FT-Raman spectroscopy as shown in Fig. 2a. Two peaks were identified at 1348 cm^{-1} and 1584 cm^{-1} . Two distinct peaks, around 1360^{-1} and 1580 cm^{-1} , were found for the graphene. The former occurs due to the breathing of sp^2 hybridized carbon, while the latter is due to the graphitic sp^2 carbon. The peak at 1348 cm^{-1} corresponds to D bands and at 1584 cm^{-1} to G bands.²⁷ Figure 2b and c show the SEM images of the LEG. Wrinkled sheets randomly oriented are seen in the SEM images. TEM images were taken to analyse the morphology in detail. Graphene has crumpled sheet morphology with few layers stacked together. Few-layer graphene often appears to be transparent as per our previous works.^{28–30} A similar trend of the nanosized sheet with wrinkling and folding at the edges was also observed in the present study (TEM images of LEG-Fig. 2 d–f). Few layers of graphene were observed stacking with each other.

Electrochemical Impedance Spectroscopy with Different Concentrations of BPE

PVP has a pyrrolidone ring, which serves as the proton acceptor because of the presence of the carbonyl group. PVA contains a proton donor hydroxyl group, so hydrogen bonding between PVP

and PVA may occur. The improved ionic conductivity of the PVP electrolyte was attributed to the plasticizing and coordinating effects. Different ratios of PVP and PVA (90:10, 80:20, 70:30, 60:40, and 50:50) were initially taken to test the formation of the film. However, it was found that if the percentage of PVP was greater than 60%, then there was no possibility of film formation, as the obtained film was brittle above this percentage of PVP. Hence, the percentage of PVP was optimized for 60%.

Figure 3 shows the Nyquist plots of the BPE with different blend polymer and KI compositions. The plot has two regions. The first is the intercept of the impedance curve on the real axis at the high-frequency region, termed the equivalent series resistance. The second is the linear curve on the lower frequency region representing the charge transfer resistance (R_{ct}). With an increase in the concentration of KI, the charge transfer resistance decreased (Fig. 3b, c). The semicircle loop of BPE-3 as shown in Fig. 3c was significantly reduced when compared to the other two compositions (Fig. 3a, b). The reduced width in the semicircle of BPE-3 composition was due to the shortened path for electron transport within the electrode material. However, this trend was not observed in BPE-4. The R_{ct} was found to increase (Fig. 3d) after the 70:30 ratio. In addition, a vertical line at the mid-frequency region, representing the conducting behaviour, was observed only in the case of BPE-3.

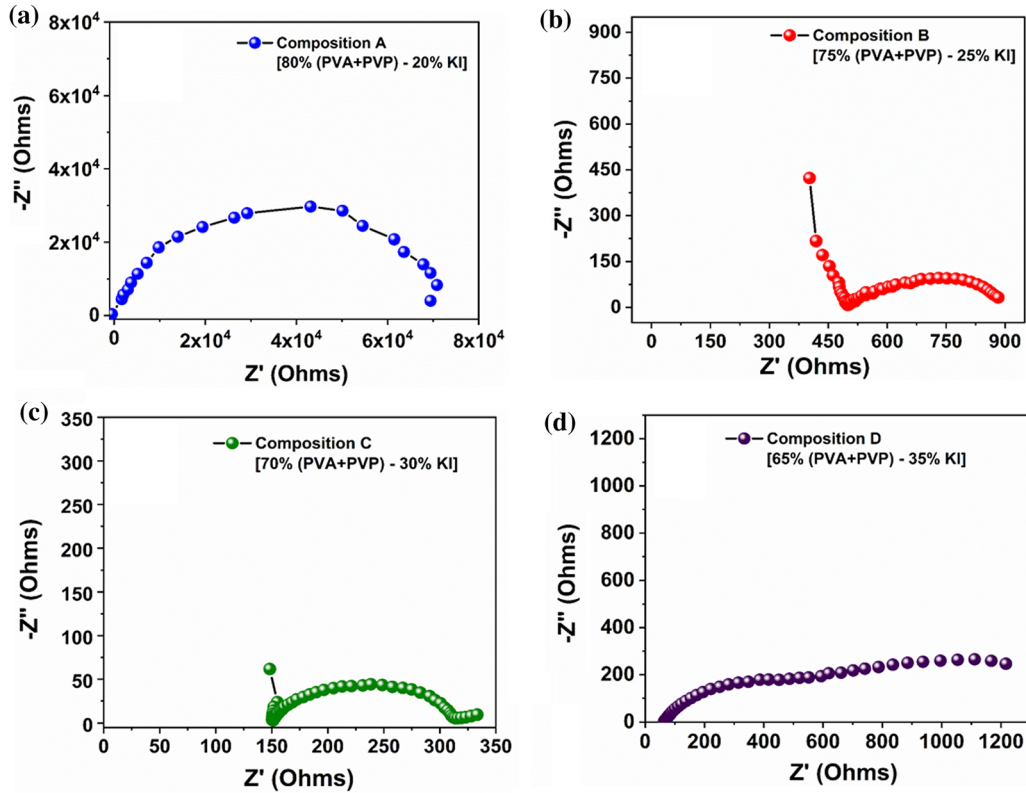


Fig. 3. Nyquist plot of blend polymer electrolytes: (a) BPE-1 (composition A: 80% (PVA + PVP)/20% KI); (b) BPE-2 (composition B: 75%(PVA + PVP)/25% KI); (c) BPE-3 (composition C: 70% (PVA + PVP)/30% KI); and (d) BPE-4 (composition D: 65% (PVA + PVP)/35% KI).

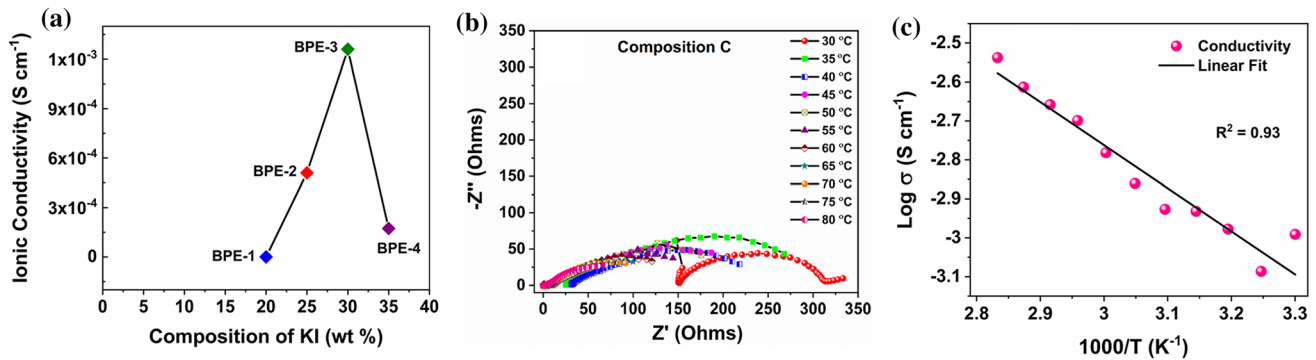


Fig. 4. (a) Ionic conductivity of four different blend polymer electrolytes as a function of KI weight percent; (b) Nyquist plots of BPE-3 at different temperatures; and (c) log conductivity vs $1000/T$ of BPE-3 different temperatures.

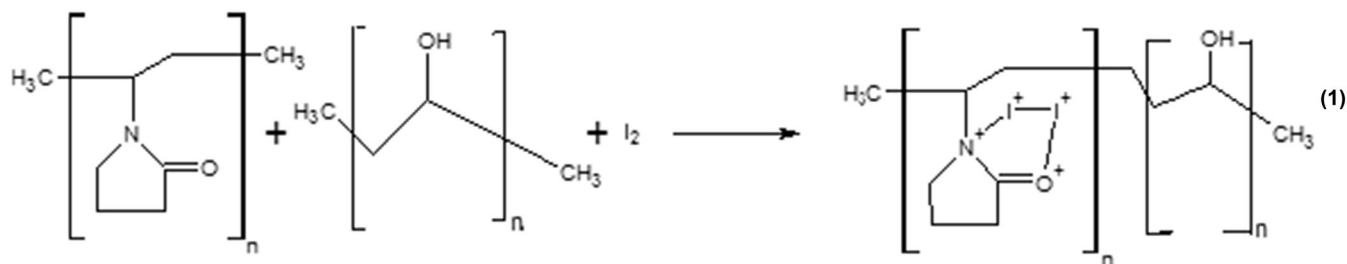
Further, as shown by the conductivity trend in Fig. 4a, the conductivity value increased from BPE-1 to BPE-3, after which the value decreased. The composition of 70:30 of PVP-PVA: KI- I_2 or BPE-3 has minimum resistance (both solution and charge transfer resistance) and hence the highest conductivity compared to the other three composites, as shown in Table I. Hence, this ratio of BPE-3 (70:30 of PVP-PVA: KI- I_2) was chosen for further studies.

In the preparation of PVP-PVA blended electrolyte, potassium iodide (KI) and iodine (I_2) were added, as it forms tri-iodide (I_3^-) ions. These ions are responsible for the charge transfer process to

the electrolyte. As the concentration of iodine was increased, the I_3^- concentration also increased. From the tri-iodide ions, polymer electrolyte (PVP) takes up I_2 ions and forms a complex as shown in Eq. 1, and I^- ions are left free for the conductivity of the electrolyte. Hence, with an increase in the concentration of iodine, there was an increase in the concentration of iodide conductivity of the film as well. By examining Fig. 3 carefully, the linear part is not seen in the BPE-1, BPE-2, and BPE-4 (composition A, B, and C). This indicates the conductive behaviour of BPE-3.

Table I. Values of series resistance and charge transfer resistance for different compositions

Concentration	Solution resistance (Ω)	Charge transfer resistance (Ω)	Ionic conductivity ($S\text{ cm}^{-1}$)
BPE-1: Composition A—80% (PVA + PVP)/20% KI	1566	67×10^3	1.27×10^{-6}
BPE-2: Composition B—75% (PVA + PVP)/25% KI	502	383	5.10×10^{-4}
BPE-3: Composition C—70% (PVA + PVP)/30% KI	150	163	1.26×10^{-3}
BPE-4: Composition D—65% (PVA + PVP)/35% KI	61	1145	1.73×10^{-4}



With lower solution/charge transfer resistance and the highest ionic conductivity among the compositions, BPE-3 represents a good polymer electrolyte for DSSC and supercapacitor applications.

Electrochemical Impedance Spectroscopy of the BPE-3 (Composition C) of the BPE at Different Temperatures

In Fig. 4b, a Nyquist plot of BPE-3 is shown for a range of temperatures (30°C to 80°C). The plot shows a semicircle trend at all temperatures. However, the radius of the semicircle varies. As the temperature rises, there is eventually a decrease in the semicircle radius, implying decreased values of charge transfer resistance at higher temperatures. With an increase in the temperature, there is a segmental motion of the polymer chain resulting in intra- and inter-chain ion movement: the more movement of ions, the greater the conductivity. Hence, the conductivity of the polymer electrolyte was higher at higher temperatures, and beyond 80°C the polymer loses its properties. Figure 4 c shows the log conductivity vs $1000/T$ of BPE-3 different temperatures. The ionic conductivity of the BPE-3 was determined at regular intervals in the temperature range. The increase in the conductivity is attributed to the movement of iodide ions in the polymer electrolyte. A linear dependence of the ionic conductivity across temperatures is observed. In other words, the electrolyte showed Arrhenius behaviour.

Dielectric Studies

The conductivity behaviour of the PVP-PVA blended polymer electrolytes can be further elucidated by dielectric studies. Figure 5 presents plots of the dielectric components for the blended polymer electrolytes. The dielectric constant is a measure of the stored charges. Impedance (Z^*) is a complex number; Z_R represents its real part and Z_I the imaginary part by the relation shown below.³¹

$$Z^* = Z_R + jZ_I, \quad \text{where } j = \sqrt{-1} \quad (2)$$

The dielectric constant ϵ_R , dielectric loss ϵ_I is calculated using the following equations

$$\epsilon_R = \frac{Z_I}{\omega C_0 (Z_R^2 + Z_I^2)} \quad (3)$$

$$\epsilon_I = \frac{Z_R}{\omega C_0 (Z_R^2 + Z_I^2)} \quad (4)$$

where $C_0 = \frac{\epsilon_0 A}{t}$, ϵ_0 represents permittivity of free space, A signifies electrode contact area, t the thickness of the electrolyte film and $\omega = 2\pi f$, f is the frequency in Hz.

The real and the imaginary part of the electrical modulus (M_R and M_I) is given by

$$M_R = \frac{\epsilon_R}{(\epsilon_R^2 + \epsilon_I^2)} \quad (5)$$

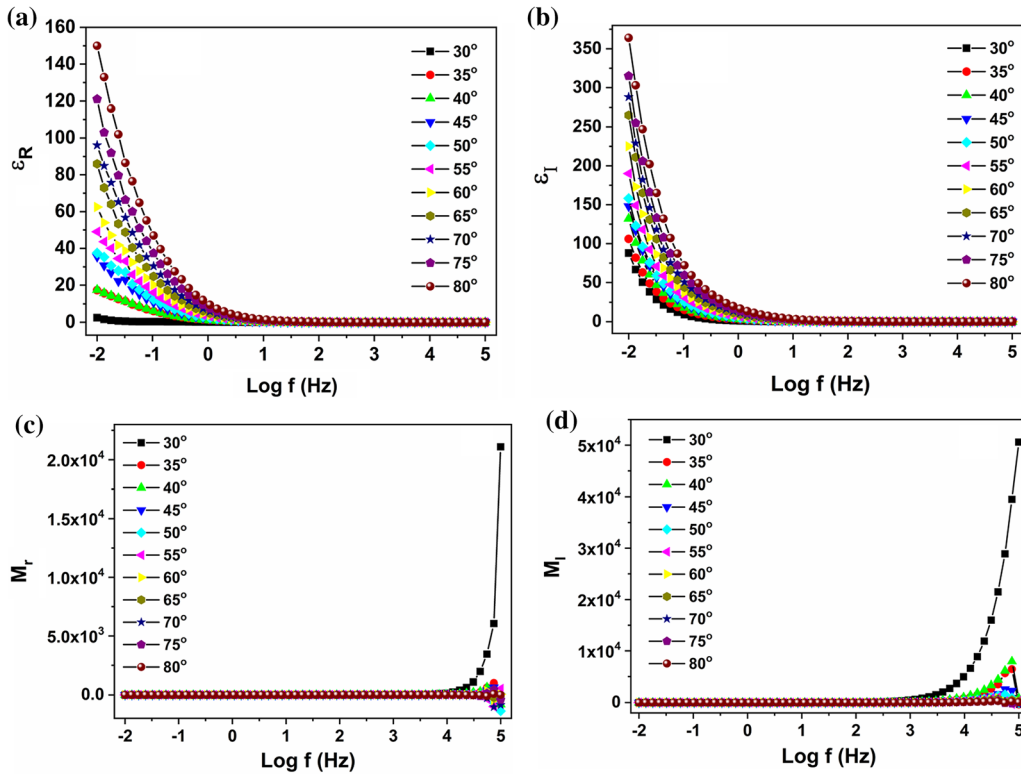


Fig. 5. Plot of (a) dielectric constant versus log f at different temperatures; (b) dielectric loss versus log f at different temperatures; (c) real part of electric modulus versus log f at different temperatures and (d) imaginary part of electric modulus versus log f at different temperatures.

$$M_I = \frac{\epsilon_I}{(\epsilon_R^2 + \epsilon_I^2)} \quad (6)$$

The dielectric study further gives a thorough idea of the electrolyte conductivity. It aids in understanding the amount of charge that will be stored in the prepared polymer electrolyte. Figure 5 exhibits the variation in ϵ_R and ϵ_I as a function of temperature. At lower frequencies, there was a sharp increase in the ϵ_R and ϵ_I . Polarisation owing to charge accumulation increases led to the observed increase in ϵ_R and ϵ_I . The plots vary distinctly from the Debye model. Both the dielectric constant and dielectric losses increase significantly at lower frequencies and increase with higher temperatures. As the temperature increases, there is a possibility for higher charge carrier and freedom of movement in all directions. That is, the degree of salt dissociation and ion aggregate re-dissociation increases the number of free ions. In other words, the density of the charge carrier is increased at higher temperatures. The values also rise sharply at low frequencies. The electrode polarization leads to a steep rise in both the constant loss. Nevertheless, in a higher frequency zone, the pattern appears to be the opposite, as both values appear to fall. This could be attributed to the rapidly occurring electrical field that could leave no excess ions for diffusion in the direction of the field applied. Figure 5c, d shows the variation of the real and imaginary part of electric

modulus, respectively. Both the real and imaginary parts of the electric modulus increase at a higher frequency. The long line-like structure observed at the lower frequency region represents the very capacitive nature of the electrolyte film. In the case of temperature measurement, however, the change in M_R and M_I values is different. Notably, even if the values are increased at a higher frequency, the peak value is located at 30 °C ambient temperature. The strong polymer electrolyte's capacitive activity is therefore optimum at room temperature of 30 °C.

Integrated Supercapacitor-Solar Cell Device Characteristics

On the FTO substrate, the supercapacitor and solar cell have been assembled. The FTO has been selected as the common platform due to its good electrical conductivity. The DSSC serves as an energy harvesting device when the entire cell is exposed to solar light. In other words, the DSSC serves as a source of power for the whole embedded cell. The dye absorbs the light in the visible zone, is excited, and injects an electron into the SnO_2 conductive band. The injected electrons enter the graphene of the counter electrode through the external load. The supercapacitor stores the produced energy from the DSSCs on combining with the DSSC cell. Figure 6a shows the current and voltage characteristics of a dye-sensitized solar cell. The intensity of the solar radiation that hits the

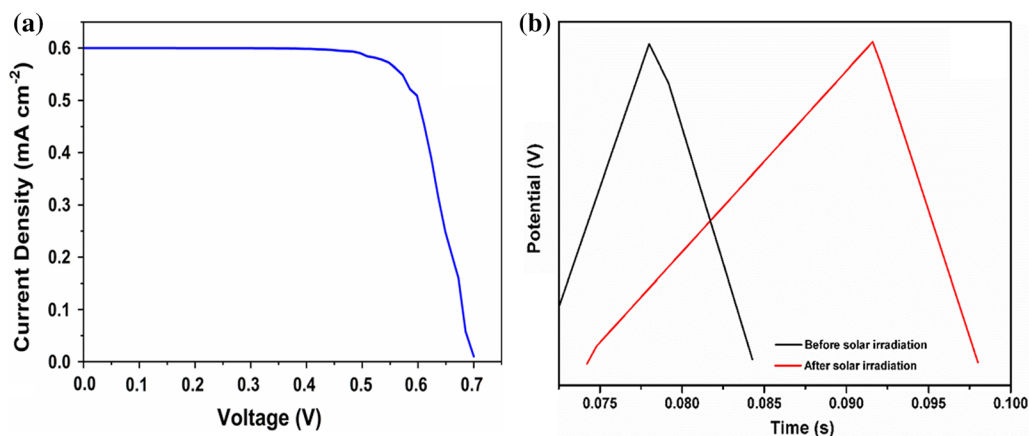


Fig. 6. (a) I-V plot of the DSSC and (b) charge-discharge graph of supercapacitor.

Table II. Comparison of the present work with the reported literature

Material	Semiconductor	Electrolyte	F.F.	η (%)	References
Red cabbage (<i>Brassica oleracea</i> var. capitata f. rubra) + Curcumin (<i>Curcuma longa</i>) (70:1)	TiO ₂	I ₂ + 1-propyl-2,3 dimethylimidazolium iodide (DMPI) + 4-tert-butyl pyridine (TBP) + propylene carbonate (PC)	0.69	0.60	32
Achiote shrub (<i>Bixa orellana</i>)	TiO ₂	I ₂ + DMPI + TBP + LiI in methoxypropionitrile	0.60	0.53	33
Black rice (<i>Oryza sativa</i> L.)	TiO ₂	KI + I ₂ in 4:1 ethylene glycol (EG) + acetonitrile	0.52		
Capsicum (<i>Capsicum annuum</i>)	TiO ₂		0.63		34
Jaboticaba (<i>Plinia cauliflora</i>)	TiO ₂	I ₂ + LiI in 90:10 acetonitrile + 3-methyl-2-oxazolidinone	0.54		
Calafate (<i>Berberis buxifolia</i> Lam)			0.36		35
Crocetin	TiO ₂	KI + I ₂ in 80:20 ethylene carbonate (EC) + acetonitrile	0.46	0.56	
Crocin of <i>Gardenia</i> fruit			0.60	0.16	36
Orange juice (<i>Citrus sinensis</i>)	TiO ₂	KI + I ₂ in 4:1 EG + acetonitrile	0.50	0.66	
Eggplant peels (<i>Solanum melongena</i>)			0.40		37
Ivy gourd (<i>C. indica</i>)	TiO ₂	I ₂ + LiI + TBP in methoxypropionitrile	0.49	0.076	
Pomegranate leaf	TiO ₂	I ₂ + LiI + TBP with dry acetonitrile	0.52	0.597	
Mulberry fruit (<i>Morus</i>)			0.53	0.548	
Mixture			0.49	0.722	39
Beetroot (<i>Beta vulgaris</i>)	TiO ₂	KI + I ₂ in 4:1 EG + acetonitrile	0.3	0.402	40
Shahkooti fruit	TiO ₂	Iodolyte ELT-ACN-I	0.73	0.32	41
Spinach (<i>Spinacia oleracea</i>)	TiO ₂	I ⁻ /I ₃ ⁻	0.58	0.17	
Onion (<i>Allium cepa</i>)			0.46	0.064	
Red Cabbage (<i>Brassica oleracea</i> var. capitata f. rubr)			0.46	0.06	42
Pomegranate (<i>Punica granatum</i>)	TiO ₂	I ⁻ /I ₃ ⁻	0.41	2.0	43
Henna leaves (<i>Lawsonia inermis</i>)	TiO ₂	KI + I ₂ in acetonitrile		1.08	
Beetroot (betanin)				1.3	44
Kokum fruit (<i>Garcinia indica</i>)	SnO ₂	KI + I ₂ in 70:30 PVP-PVA	0.42	0.56	This work

DSSC device controls the current (I), and at the same time, there is an increase in the temperature of DSSC that reduces its voltage (V). The fill factor of the integrated device calculated from this graph

was 0.42. Further, the efficiency of the DSSC was calculated to be 0.56%. Table II summarizes the comparison of the current work with the previously reported works.

Figure 6b represents the charge-discharge curve of the supercapacitor measured at a 2 mA cm^{-2} current density. The discharge time of 2 ms was observed before irradiating with sunlight. However, the discharge time prolonged to 6.4 ms after irradiating with sunlight. In the integrated device, the original value is almost three times the initial value. An increase in the discharge time indicates that (1) the solar light is trapped by the photosensitizer of DSSC, (2) charge transport takes place across the DSSC-SC through FTO and (3) graphene-graphene SCs stores charges across the electrode/electrolyte interface via electrical double layer mechanism. The photo-charge EDLC is seen as rising to a peak voltage of 3 V. However, discharging takes place much more quickly than the charging phase. Although the discharge time value is less, the operation of the device might be in short time charging/discharging units depending on user demand. An increase in discharge time certainly indicates that (1) solar light is absorbed by the DSSC photosensitizer, (2) charges are transported through the DSSC-SC via FTO, and (3) graphene-graphene SCs store charges across the electrode-electrolyte interface through the electrical double-layer formation. The specific capacitance of the device was calculated, and it was found to be 20 F g^{-1} . This article consists of an integration of DSSC and SC. Only DSSC produces energy and only SC stores energy. Separately, both devices are dependent on other sources for generating and converting energy. However, in this embedded DSSC-SC, the system is self-functioning. Energy generated in DSSC can be readily stored in SC and then used later. Therefore, these instruments are of primary importance.

CONCLUSION

SnO_2 was synthesized via a simple and fast microwave technique. The BPE film was prepared using an optimized PVP-PVA/ I_3^- electrolyte. One step-laser engraving method was used for graphene synthesis on the Kapton sheet. The dye extracted from the Kokum rind was effectively used as a photosensitizer in the fabrication of DSSC. DSSC fabricated via kokum dye-coated photoanode and graphene cathode gave a fill factor of 0.42 and an efficiency of 0.56%. After integrating DSSC with SCs, the discharge time was found to be enhanced threefold after light irradiation. The integrated DSSC-SCs gave a specific capacitance of 20 F g^{-1} . The increased charge-discharge time after solar irradiation showed that the device effectively absorbs solar energy and hence, is stored in the supercapacitor.

ACKNOWLEDGMENTS

The authors are thankful to MIT for providing the laboratory facility and also thank the central

instrumental facility of MAHE for the characterization facility.

FUNDING

Open access funding provided by Manipal Academy of Higher Education, Manipal

OPEN ACCESS

This article is licensed under a Creative Commons Attribution 4.0 International License, which permits use, sharing, adaptation, distribution and reproduction in any medium or format, as long as you give appropriate credit to the original author(s) and the source, provide a link to the Creative Commons licence, and indicate if changes were made. The images or other third party material in this article are included in the article's Creative Commons licence, unless indicated otherwise in a credit line to the material. If material is not included in the article's Creative Commons licence and your intended use is not permitted by statutory regulation or exceeds the permitted use, you will need to obtain permission directly from the copyright holder. To view a copy of this licence, visit <http://creativecommons.org/licenses/by/4.0/>.

REFERENCES

1. M.K. Nazeeruddin, E. Baranoff, and M. Grätzel, *Sol. Energy* 85, 1172 (2011).
2. J. Gong, K. Sumathy, Q. Qiao, and Z. Zhou, *Renew. Sustain. Energy Rev.* 68, 234 (2017).
3. M. Grätzel, *J. Photochem. Photobiol. C Photochem. Rev.* 4, 145 (2003).
4. M. Winter and R.J. Brodd, *Chem. Rev.* 104, 4245 (2004).
5. M. Ye, X. Wen, M. Wang, J. Iocozzia, N. Zhang, C. Lin, and Z. Lin, *Mater. Today* 18, 155 (2015).
6. B. Qiu, M. Xing, and J. Zhang, *Chem. Soc. Rev.* 47, 2165 (2018).
7. C. Xu, B. Xu, Y. Gu, Z. Xiong, J. Sun, and X.S. Zhao, *Energy Environ. Sci.* 6, 1388 (2013).
8. L. Huang, D. Santiago, P. Loyselle, and L. Dai, *Small* 14, 1 (2018).
9. J.D. Roy-Mayhew and I.A. Aksay, *Chem. Rev.* 114, 6323 (2014).
10. K. Robinson, G.R.A. Kumara, R.J.G.L.R. Kumara, E.N. Jayaweera, and R.M.G. Rajapakse, *Org. Electron. Phys. Mater. Appl.* 56, 159 (2018).
11. S.H. Lee, J.H. Kim, and J.R. Yoon, *Sci. Rep.* 8, 1 (2018).
12. F. Tehrani and B. Bavarian, *Sci. Rep.* 6, 1 (2016).
13. S. Kang, K. Lim, H. Park, J.B. Park, S.C. Park, S.P. Cho, K. Kang, B.H. Hong, and A.C.S. Appl, *Mater. Interfaces* 10, 1033 (2018).
14. D. Kumar and K.T. Wong, *Mater. Today Energy* 5, 243 (2017).
15. M.Z.H. Khan, M.R. Al-Mamun, P.K. Halder, and M.A. Aziz, *Renew. Sustain. Energy Rev.* 71, 602 (2017).
16. N.K. Zainuddin, N.M.J. Rasali, N.F. Mazuki, M.A. Saadiah, and A.S. Samsudin, *Int. J. Hydrogen Energy* 45, 8727 (2020).
17. N.F. Mazuki, A.P.P. Abdul Majeed, Y. Nagao, and A.S. Samsudin, *Polym. Test.* 81, 106234 (2020).

18. S. Jayanthi, *Adv. Compos. Hybrid Mater.* 2, 351 (2019).
19. S.B. Aziz, M.H. Hamsan, R.M. Abdullah, and M.F.Z. Kadir, *Molecules* 24, 2503 (2019).
20. K.S. Ngai, S. Ramesh, K. Ramesh, and J.C. Juan, *Ionics (Kiel)* 22, 1259 (2016).
21. P. Dong, M.T.F. Rodrigues, J. Zhang, R.S. Borges, K. Kalaga, A.L.M. Reddy, G.G. Silva, P.M. Ajayan, and J. Lou, *Nano Energy* 42, 181 (2017).
22. A. Scalia, F. Bella, A. Lamberti, S. Bianco, C. Gerbaldi, E. Tresso, and C.F. Pirri, *J. Power Sources* 359, 311 (2017).
23. C.A. Nayak, N.K. Rastogi, and K.S.M.S. Raghavarao, *Int. J. Food Prop.* 13, 441 (2010).
24. R.C. Ranveer and A.K. Sahoo, *Nutr. Food Toxicol.* 1, 236 (2017).
25. B. Miguel, A. Shirodkar, D.J. Bhat, and S. Krishnan, eds., *Resource book on kokum (Garcinia indica Choisy) Issue No. 3* (Western Ghats Kokum Foundation, 2012), p. 120.
26. S.B. Swami, N.J. Thakor, and S.C. Patil, *J. Food Res. Technol.* 2, 130 (2014).
27. J. Wu, M. Lin, X. Cong, H. Liu, and P. Tan, *Chem. Soc. Rev.* 47, 1822 (2018).
28. Y.N. Sudhakar, M. Selvakumar, D.K. Bhat, and S. Senthil Kumar, *RSC Adv.* 4, 60039 (2014).
29. Y.N. Sudhakar, H. Hemant, S.S. Nitinkumar, P. Poornesh, and M. Selvakumar, *Ionics (Kiel)* 23, 1267 (2017).
30. Shruthi, K.M. Vighnesha, Sandhya, D.N. Sangeetha, and M. Selvakumar, *Surf. Eng. Appl. Electrochem.* 54, 359 (2018).
31. Y.N. Sudhakar and M. Selvakumar, *J. Appl. Electrochem.* 43, 21 (2013).
32. S. Furukawa, H. Iino, T. Iwamoto, K. Kukita, and S. Yamauchi, *Thin Solid Films* 518, 526 (2009).
33. N.M. Gómez-Ortíz, I.A. Vázquez-Maldonado, A.R. Pérez-Espadas, G.J. Mena-Rejón, J.A. Azamar-Barrios, and G. Oskam, *Sol. Energy Mater. Sol. Cells* 94, 40 (2010).
34. S. Hao, J. Wu, Y. Huang, and J. Lin, *Sol. Energy* 80, 209 (2006).
35. A.S. Polo and N.Y. Murakami Iha, *Sol. Energy. Mater. Sol. Cells* 90, 1936 (2006).
36. E. Yamazaki, M. Murayama, N. Nishikawa, N. Hashimoto, M. Shoyama, and O. Kurita, *Sol. Energy* 81, 512 (2007).
37. G. Calogero and G. Di Marco, *Sol. Energy Mater. Sol. Cells* 92, 1341 (2008).
38. V. Shanmugam, S. Manoharan, S. Anandan, and R. Murugan, *Spectrochim. Acta Part A Mol. Biomol. Spectrosc.* 104, 35 (2013).
39. H. Chang and Y.J. Lo, *Sol. Energy* 84, 1833 (2010).
40. C.I. Oprea, A. Dumbrava, I. Enache, A. Georgescu, and M.A. Girtu, *J. Photochem. Photobiol. A Chem.* 240, 5 (2012).
41. S.A. Mozaffari, M. Saeidi, and R. Rahmanian, *Spectrochim. Acta Part A Mol. Biomol. Spectrosc.* 142, 226 (2015).
42. A.M. Ammar, H.S.H. Mohamed, M.M.K. Yousef, G.M. Abdel-Hafez, A.S. Hassanien, and A.S.G. Khalil, *J. Nanomater.* 2019, 1 (2019).
43. W. Ghann, H. Kang, T. Sheikh, S. Yadav, T. Chavez-Gil, F. Nesbitt, and J. Uddin, *Sci. Rep.* 7, 1 (2017).
44. S. Sathyajothi, R. Jayavel, and A.C. Dhanemozhi, *Mater. Today Proc.* 4, 668 (2017).

Publisher's Note Springer Nature remains neutral with regard to jurisdictional claims in published maps and institutional affiliations.